



Penetration of a spherical vortex into turbulence

Ian Eames^{1,†} and Jan-Bert Flór²

¹University College London, Gower Street, London WC1E 6B, UK

²LEGI, Laboratoires des Ecoulements Geophysiques et Industriels BP 53, 38041 Grenoble CEDEX 09, France

(Received 27 October 2023; revised 17 May 2024; accepted 27 June 2024)

The penetration of a spherical vortex into turbulence is studied theoretically and experimentally. The characteristics of the vortex are first analysed from an integral perspective that reconciles the far-field dipolar flow with the near-field source flow. The influence of entrainment on the vortex drag force is elucidated, extending the Maxworthy (*J. Fluid Mech.*, vol. 81, 1977, pp. 465–495) model to account for turbulent entrainment into the vortex movement and vortex penetration into an evolving turbulent field. The physics are explored numerically using a spherical vortex (initial radius R_0 , speed U_{v0}), characterised by a Reynolds number $Re_0 (= 2R_0U_{v0}/\nu$, where ν is the kinematic viscosity) of 2000, moving into decaying homogeneous turbulence (root-mean-square u_0 , integral scale L) with turbulent intensity $I_t = u_0/U_{v0}$. When the turbulence is absent ($I_t = 0$), a wake volume flux leads to a reduction of vortex impulse that causes the vortex to slow down. In the presence of turbulence ($I_t > 0$), the loss of vortical material is enhanced and the vortex speed decreases until it is comparable to the local turbulent intensity and quickly fragments, penetrating a distance that scales as I_t^{-1} . In the experimental study, a vortex ($Re_0 \sim 1490$ – 5660) propagating into a statistically steady, spatially varying turbulent field ($I_{ve} = 0.02$ to 0.98). The penetration distance is observed to scale with the inverse of the turbulent intensity. Incorporating the spatially and temporally varying turbulent fields into the integral model gives a good agreement with the predicted trend of the vortex penetration distance with turbulent intensity and insight into its dependence on the structure of the turbulence.

Key words: vortex breakdown, vortex interactions, vortex shedding

1. Introduction

Vortex rings, dipoles and line vortices (see Pullin & Saffman 1998) are fundamental components of turbulence (see Synge & Lin 1943; Saffman 1997). As these

† Email address for correspondence: i.eames@ucl.ac.uk

vortical structures are basic elements of complex flows, their interactions with flow inhomogeneities provide a crucial starting point for exploring fundamental flow processes. In this paper, we investigate the interaction between a vortex ring and turbulence as an initial step toward examining critical layers between regions of turbulence.

The pivotal advance in understanding the dynamics of turbulent vortex rings came from Maxworthy's (1974) interpretation of Osborne Reynolds' observation that vortices lose mass and slow down. Figure 1(a) (see also figure 10, discussed later) depicts a turbulent vortex propagating into a quiescent flow, with the mass loss evident from the detrainment of dyed fluid behind the vortex, as is discussed in more detail in § 6. This mass loss leads to a decrease in the vortex impulse and a reduction in the vortex speed, which are often incorrectly interpreted as a drag force. This interpretation has a wider significance beyond the dynamics of vortices, such as in problems where entrainment exerts an equivalent force (or impulse decrease) that occurs even in the absence of solid boundaries. Maxworthy (1974) noted that vortex progression in stationary fluids is not universally consistent over time but develops through well-defined sequential steps, each with distinct scaling laws.

While most idealised studies have considered a vortex propagating in a quiescent flow, real-world scenarios typically involve some level of ambient turbulence affecting the longevity and persistence of these structures. Many related studies have considered well-behaved laminar vortex rings in an ambient fluid at rest, dominated by a diffusive dynamics and relatively small entrainment effects (see e.g. recent works such as Tinaikar, Advait & Basu 2018, and references therein). Maxworthy (1977) demonstrated how external processes like buoyancy, stratification and turbulence, dramatically influence a vortex's lifetime. Arnold (1974) conducted the first detailed experimental study of a vortex ring moving into turbulence created in a water channel. The vortices were observed to grow faster in size and slow down more rapidly due to the background turbulence (Arnold 1974; Maxworthy 1977). Although the reduction of the vortex speed and increase in vortex radius were evident, the final stages of the vortex propagation and arrestment were not observed. This forms an essential component of this study.

Several relevant studies have examined vortices interacting with turbulence, including experimental and theoretical studies of line vortices created by a lifting surface in a turbulent flow (see van Jaarsveld *et al.* 2011), and a single line vortex interacting with turbulence (Marshall & Beninati 2005). The latter example demonstrated the critical change in the external turbulence structure caused by the differential rotation imparted by the line vortex. The case of a propagating three-dimensional vortex is quite different from monopolar and line vortices owing to the flow perturbation decaying more rapidly with distance and the vorticity maximum (within the vortex) lying close to the bounding streamline.

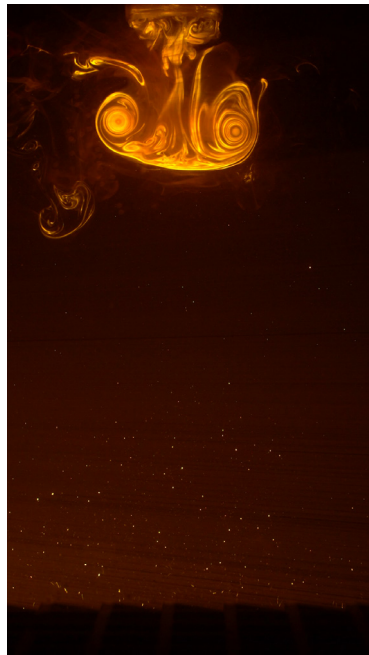
In this paper, we address a key missing element in the vortex dynamics: the interaction between a spherical vortex and turbulence. The dramatic effect of turbulence on a vortex is shown by contrasting figures 1(a,b) with figures 1(c,d). The turbulence significantly decreases the vortex speed by enhancing the growth of the vortex size through enhanced entrainment by the external turbulence and loss of vortical fluid in the vortex wake. Part of the challenge of incorporating the effect of turbulence into the description of the vortex is to understand the distinction between enhanced entrainment across the vortex edge and its influence on the overall 'force' experienced by the vortex. An integral perspective gives greater clarity about the different effects of entrainment and detrainment on the vortex properties, helping to reconcile the dipolar nature of the vortex with the monopolar flow created by the loss of impulse. Drawing on Maxworthy (1977), the additional effect of a spatially and temporally varying turbulent field on the vortex is proposed and analysed.

Penetration of a spherical vortex into turbulence

(a)



(c)



(b)



(d)

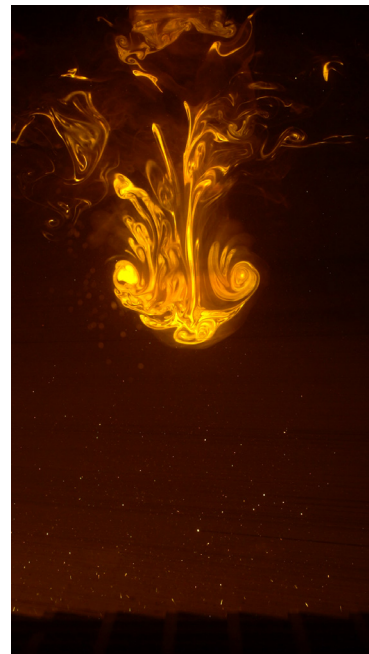


Figure 1. Visualisation of a ring vortex moving steadily into (a,b) a quiescent flow and (c,d) a turbulent field generated by an oscillating grid, both at 4.6 and 17.0 s, respectively, after vortex generation. The Reynolds number of the initial vortex, based on velocity and distance between the vortices, is 3200. Experimental parameters correspond to experiment *T* in table 1. The image is 50 cm wide.

Numerical simulations are performed on the idealised interaction of a Hill’s spherical vortex moving into decaying homogeneous turbulence. An analysis of the dynamics requires the development of both Lagrangian and Eulerian measures of impulse and momentum, which are intrinsically linked to the integral perspective offered.

An experimental study is developed to examine the vortex penetration into a turbulent flow (see [figure 1](#)) with the fundamental difference between the numerical and experimental study being the turbulence distribution. In the experimental study, a piston-driven vortex is generated that moves into a grid-generated turbulent flow field. The strength of the turbulence is sufficiently high that a finite penetration distance of the vortices is realised, in contrast to the experiments of Arnold, Klettner & Eames (2013), where the level of turbulence is weak. The two strands of study are brought together through a comparison with the integral vortex model.

The paper is structured as follows. In continuation of the introduction, to analyse the gross features of the interaction, integral measures are introduced (in § 2), which provides an opportunity to elaborate on Maxworthy’s model, in particular the role of entrainment in the rate of change of impulse and extension to incorporate the effect of external turbulence on the vortex dynamics. The computational and experimental methodologies are described in §§ 3 and 4, respectively. The basic building block of a spherical vortex moving through a quiescent region is analysed in § 5, focusing not just on the vortical dynamics but also how fluid elements external to the vortex are displaced and distorted. In § 6, the numerical and experimental results are analysed. The primary results concern the relationship between penetration distance into turbulence and the turbulent structure, which is discussed using the integral model. Finally, the results are put into a general context in § 7.

2. Integral measures of the flow processes

2.1. Integral measures

Integral measures of momentum, impulse, circulation and kinetic energy are useful for analysing the gross dynamics of complex flows, even for processes involving changes in flow topology (Benjamin & Ellis 1966; Eames 2008). A challenge of using these measures is that they may need to be reconciled for the presence of flow boundaries (Theodorsen 1941; Darwin 1953; Eames, Belcher & Hunt 1994). A key measure is the impulse associated with a region of the flow. The specific impulse of a vortical element within the region is proportional to the weighted integral of the moment of vorticity ($\boldsymbol{\omega}$)

$$\mathbf{I} = \frac{1}{2} \mathbf{x} \times \boldsymbol{\omega}, \tag{2.1}$$

where the vorticity is defined as $\boldsymbol{\omega} = \nabla \times \mathbf{u}$, where \mathbf{u} is the velocity field and \mathbf{x} is position. For three-dimensional flows impulse changes at a rate

$$\frac{D\mathbf{I}}{Dt} = \mathbf{u} \times \boldsymbol{\omega} + \frac{1}{2} \boldsymbol{\omega} \cdot \nabla (\mathbf{x} \times \mathbf{u}) + \frac{1}{2} \mathbf{x} \times \nu \nabla^2 \boldsymbol{\omega}, \tag{2.2}$$

which includes the diffusion of vorticity with ν the kinematic viscosity. Half of the contribution to the vortex force ($\mathbf{u} \times \boldsymbol{\omega}$) comes from the advection of the vorticity while the other half comes from stretching. The two remaining terms come from the production of stretching of vorticity by angular momentum and the diffusion of vorticity. The specific

impulse associated with free vorticity in a region V is

$$\mathbf{I}_v = \int_V \frac{1}{2} \mathbf{x} \times \boldsymbol{\omega} \, dV. \quad (2.3)$$

The rate of change of total impulse in a control volume V , whose boundary S moves with velocity \mathbf{u}_b , can be evaluated by using the result of Saffman (1995, ch. 3.2, (10) and (11)) and the Reynolds transport theorem

$$\begin{aligned} \frac{d\mathbf{I}_v}{dt} &= \int_V \mathbf{u} \times \boldsymbol{\omega} \, dV + \int_S \frac{1}{2} ((\boldsymbol{\omega} \cdot \hat{\mathbf{n}}) \mathbf{x} \times \mathbf{u} - (\mathbf{u} \cdot \hat{\mathbf{n}}) (\mathbf{x} \times \boldsymbol{\omega})) \, dS \\ &+ \int_S (\mathbf{u}_b \cdot \hat{\mathbf{n}}) \left(\frac{1}{2} \mathbf{x} \times \boldsymbol{\omega} \right) \, dS + \int_V \frac{1}{2} \mathbf{x} \times \nu \nabla^2 \boldsymbol{\omega} \, dV, \end{aligned} \quad (2.4)$$

where $\hat{\mathbf{n}}$ is a unit vector pointing out of the control volume. For a large domain that encloses a compact region of vorticity, the second and third integrals are zero and the change in impulse is then expressed in terms of the total vortex force imposed on the flow. As Saffman discusses, the consequence of the far-field flow being dipolar is that the impulse and dipole moment – which are intrinsically linked – are conserved/constant.

Our attention is on the behaviour of a vortex propagating and disintegrating as it penetrates a turbulent flow. To distinguish between the vortex and the external turbulence, we make use of a passive scalar field C and Lagrangian fluid particles to tag the vortex. The passive scalar is set to be $C = 1$ within the vortex (of volume V_0) and zero outside. The Lagrangian perspective is developed by tagging N_p fluid particles initially within the vortex. The integral measures of A , based on either a Lagrangian or Eulerian approach are defined as

$$A^{(L)} = \frac{1}{N_p} \sum_{i=1}^{N_p} A(\mathbf{X}_i), \quad A^{(E)} = \frac{1}{V_0} \int_V CA(\mathbf{x}, t) \, dV, \quad (2.5a,b)$$

respectively, and distinguished by the superscript L or E (see Eames, Hunt & Belcher 2004). The Eulerian and Lagrangian measures of vortex impulse, $\mathbf{I}_v^{(E)}$ and $\mathbf{I}_v^{(L)}$, respectively, are defined in terms of $A = \frac{1}{2} \mathbf{x} \times \boldsymbol{\omega}$.

2.2. Integral vortex model

In this section, the vortex dynamics are analysed from an integral perspective that requires distinguishing between the vorticity that forms the main body of the vortex and that which is deposited downstream. This distinction requires a separation of scales between the size of the vortex and the distance over which the vortex has travelled. There are several ways to identify the position of the vortex, including weighted measures of the initial constituent material of the vortex and positions of local maxima of vorticity magnitude; for consistency with the numerical calculations and experiments, the vortex centre \mathbf{X}_v is defined by following the initial fluid within the vortex (with $A = \mathbf{x}$ in (2.5a,b)); the superscript (L) is dropped. For the numerical simulation, the position is determined by following (Lagrangian) fluid particles in time, while for the experiments, the dye is followed in time. The vortex velocity, \mathbf{U}_v , is defined as $d\mathbf{X}_v/dt$.

For unbounded flows, the dipole moment in the far field is unchanged in time, but this needs to be reconciled with changes that occur in the vicinity of the vortex. Maxworthy (1974) argued that the progressive loss of mass, evident through a visible wake loss, leads to the vortex impulse decreasing in time. The integral analysis is applied over a volume

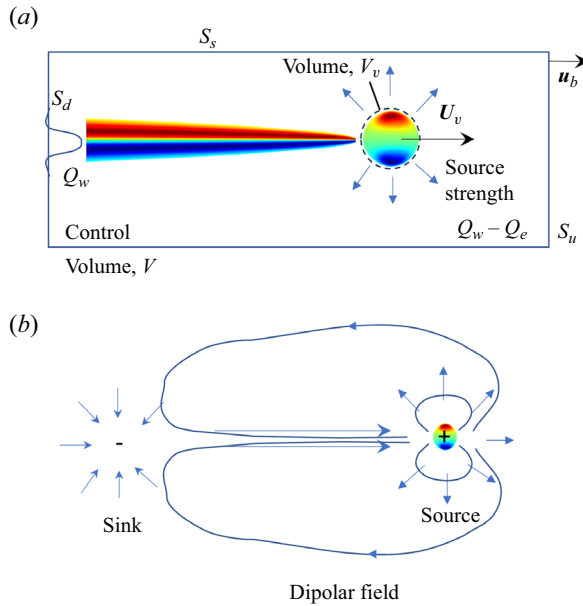


Figure 2. (a) Schematic of the control volume V and surface S , moving with speed U_v with the vortex that is used in the analysis. (b) The flow perturbation associated with the vortex moving from rest is characterised by a sink at the start and local source flow (due to the loss of impulse) which reconciles the far-field dipolar flow with the near-field monopolar flow, and this is shown as a schematic.

V that has a size larger than the size of the vortex, e.g. $O(V_v^{1/3})$ (where V_v is the volume of the vortex), and moving with velocity $u_b = U_v \hat{x}$ (figure 2a). Identifying $I_v = I_v \cdot \hat{x}$ as the local impulse associated with the vortex, Maxworthy (1974) argued that, at high Reynolds numbers, the third term in (2.4) was dominant, with the rate of change of the vortex impulse being

$$\frac{dI_v}{dt} \approx -\frac{1}{2} \int_{S_d} U_v \sigma \omega_\phi dS, \quad (2.6)$$

where σ is the radial distance from the centreline, ω_ϕ is the azimuthal vorticity component and the integration is taken over the downstream surface S_d (see figure 2a). Equation (2.6) can be written as

$$\frac{dI_v}{dt} \approx -Q_w U_v, \quad Q_w = \int_{S_d} \frac{1}{2} \sigma \omega_\phi dS, \quad (2.7a,b)$$

where Q_w is the volume flux (deficit) behind the vortex. The volume flux generates a monopolar flow in the near field (figure 2b). The combination of the sink flow created by the vortex starting, and the source flow created by drag, yields a far-field flow which is dipolar in character. These types of source–sink flows are also created by rigid bodies impulsively set into motion; Hinch provides an extremely clear physical interpretation of the consequence of these impulsively driven flows on the forces experienced by moving bodies in Appendix D of Lovalenti & Brady (1993).

The importance of the remaining terms in (2.4) was not discussed by Maxworthy and needs more analysis to unpick their link to the flow physics. Entrainment is in general mechanistically distinguished as having either an inviscid or a viscous component (da Silva *et al.* 2014). The (inviscid) engulfment process leads to a net flow across an interface, while

the viscous mechanism leads to boundary movement with a generally weaker boundary velocity. Without defining the features of such processes, we ascribe the flow due to entrainment as a volume flux, Q_e , and the loss of vorticity in the wake being equivalent to a volume flux Q_w . Due to the combination of the wake flow and entrainment, the flow in the region moving with the vortex ($R_0 \ll |x - X_v| \ll |X_v|$) is, to leading order,

$$\mathbf{u} \sim -U_v \hat{\mathbf{x}} + \frac{Q_w - Q_e}{4\pi} \frac{\mathbf{x} - \mathbf{X}_v}{|\mathbf{x} - \mathbf{X}_v|^3}, \quad (2.8)$$

where the vortex position X_v may be defined in terms of the position of the original constituent fluid. We can use (2.8) to evaluate (2.4) more precisely than (2.6). The components of the control surfaces that bound the sides of the cylinder S_s , the upstream surface S_u and the surface for the downstream wake, S_d , can be distinguished (see figure 2a). The vorticity is zero everywhere on S_s except on the surface S_d . Typically, $\boldsymbol{\omega}$ is perpendicular to the direction of motion so that $(\boldsymbol{\omega} \cdot \hat{\mathbf{n}} = 0)$. Using

$$\mathbf{u} \times \boldsymbol{\omega} = -(\mathbf{u} \cdot \nabla)\mathbf{u} + \nabla \left(\frac{1}{2}q^2 \right), \quad (2.9)$$

where $q = |\mathbf{u}|$, the rate of change of impulse can be written as

$$\frac{d\mathbf{I}_v}{dt} = \int_{S_s+S_u+S_d} -(\mathbf{u} \cdot \hat{\mathbf{n}})\mathbf{u} \, dS + \int_{S_d} \left(\frac{1}{2}q^2 \hat{\mathbf{n}} - \frac{1}{2}(\mathbf{u} \cdot \hat{\mathbf{n}})(\mathbf{x} \times \boldsymbol{\omega}) \right) dS. \quad (2.10)$$

For an axisymmetric flow characterised by a large gradient in the cross-stream direction, $\omega_\phi = -\partial u_x / \partial \sigma$, which means that the last integral is zero. Using (2.9), the first integral over both control surfaces, S_s and S_u , gives rise to a $(Q_w - Q_e)U_v$ term. In total, the rate of change of the vortex impulse is

$$\frac{d\mathbf{I}_v}{dt} = (Q_w - Q_e)U_v - 2Q_w U_v. \quad (2.11)$$

The physical interpretation follows the discussion of Hunt & Eames (2002) and Eames & Hunt (2004) – the source term gives rises to a Lamb thrust force $(Q_w - Q_e)U_v$, while the momentum flux in the wake generates a drag $-2Q_w U_v$. Thus, the change in the local vortex impulse (2.11) becomes

$$\frac{d\mathbf{I}_v}{dt} = -(Q_w + Q_e)U_v, \quad (2.12)$$

with entrainment now accounted for in this new description. This explanation provides the first clear and consistent link between the wake-drag model of Maxworthy and the entrainment drag law discussed in the context of cross-flow jets (see Coelho & Hunt (1989) for a discussion of the key physics for strong cross-flow jets). The consequence of the local flow being dominated by a source (2.8) is still consistent with the global perspective of a far-field dipole moment. Taking into account the loss of impulse and its change along the vortex path is equivalent to a line distribution of sinks whose total sum is equal to $Q_e - Q_w$, as shown in figure 2(b). The global impulse, created by the trailing wake and the head of the vortex, is thus conserved.

The volume flux can be expressed in terms of an average wake flow U_w and equivalent wake radius R_w

$$Q_w = \pi R_w^2 U_w. \quad (2.13)$$

Maxworthy (1974) interpreted the volume flux as an equivalent drag force $F_D = \rho U_v Q_w$ to which he ascribed an equivalent drag coefficient $C_Q = 2Q_w / \pi R_w^2 U_v$. The wake width

behind a vortex R_w is expected to be smaller than that behind a solid sphere because the growth of the vortex wake width is due to significant negative strain at its rear rather than due to boundary layer separation, so that $R_w/R_0 = \beta$. With the velocity deficit $U_w/U_v = \eta$, these estimates can be combined into

$$Q_w = \beta^2 \eta \pi R^2 U_v, \tag{2.14}$$

so that $C_Q = 2\beta^2 \eta$. The wake width is still much narrower than that of a rigid body with estimated values $\beta \sim 1/3$ and $\eta \sim 1/4$. An *a priori* estimate of $C_Q \sim 0.12$ is close to the value $C_Q = 0.1$ that Maxworthy inferred from lines of fit to his experimental data. To account for the growth of the vortex, Maxworthy (1974) introduced an additional integral equation describing the increase in volume due to an effective entrainment rate α

$$\frac{dV_v}{dt} = Q_w = 4\pi\alpha R_v^2 U_v, \tag{2.15}$$

based on generalising the entrainment concept of Morton, Taylor & Turner (1956). Here, entrainment is ascribed over the whole surface of the vortex and $C_Q = 8\alpha$. Maxworthy (1974) defined a lumped parameter $C_D = C_Q/4\alpha$ which was determined to have a value that spanned from 1.9 to 2.7 in his tests. The growth of the vortex arises due to the wake volume flux (Q_w) and entrainment ($Q_e + Q_w$), that gives an effective entrainment coefficient $\alpha = C_Q/8$. This closure gives a fixed value of $C_D = 2$ which sits in the range estimated by Maxworthy (1974). This also explains why the effective entrainment rate is in the range $\alpha \sim 0.010\text{--}0.0012$ (see Maxworthy 1977, figure 24, and table 1), i.e. by an order of magnitude smaller than the entrainment coefficient of a jet, which is typically $\alpha \sim 0.065\text{--}0.08$ (see van Reeuwijk & Craske 2015).

2.3. Interaction with turbulence

The bulk model of vortex movement, described by Maxworthy (1974), is developed to include the approximate effects of external turbulence on the vortex dynamics. This proves a fruitful avenue to pursue because it enables the influence of a spatially and temporally varying turbulent field on the gross dynamics of a vortex to be assessed. The external turbulence is effective at dispersing material shed behind the vortex but this influence on the vortex impulse is of secondary importance compared with the growth of the vortex through entrainment. The effect of external turbulence on the vortex is parameterised in terms of its entrainment through the vortex surface ($S_v = 4\pi R_v^2$)

$$Q_e = S_v \alpha_e u_e. \tag{2.16}$$

The growth of the vortex occurs through entrainment caused by the turbulence exterior to the vortex surface and the wake volume flux, a process which is parameterised by

$$\frac{dV_v}{dt} = Q_e + Q_w. \tag{2.17}$$

The impulse of the vortex is

$$I_v = (1 + C_m) U_v V_v, \tag{2.18}$$

Penetration of a spherical vortex into turbulence

and for an approximately spherical vortex, $C_m = 1/2$ (Saffman 1995). Combined with (2.12), this means that the dynamics of the vortex is described by

$$\frac{dR_v}{dt} = \alpha_e u_e(x, t) + \alpha U_v, \tag{2.19}$$

$$\frac{dU_v}{dt} = -\frac{2 + C_m}{1 + C_m} \frac{U_v(Q_w + Q_e)}{V_v}, \tag{2.20}$$

$$\frac{dX_v}{dt} = U_v. \tag{2.21}$$

The model (2.19)–(2.21) differs from Maxworthy (1974) with the inclusion of the effect of entrainment caused by external turbulence that is included in (2.19) and (2.20). Combining (2.20) and (2.17) gives

$$\frac{U_v}{U_{v0}} = \left(\frac{R_v}{R_0}\right)^{-5}, \tag{2.22}$$

regardless of how the turbulent intensity varies in time or space. The influence of external turbulence is parameterised to have an external entrainment coefficient, $\alpha_e \sim 0.12$, that is more typical of turbulent jets (e.g. van Reeuwijk & Craske 2015), and the internal entrainment coefficient taken to be $\alpha \sim 0.012$, which was inferred by Maxworthy (1977) from the growth of the size of the turbulent vortex.

The dynamics of a dipolar vortex can be understood by integrating the coupled system of (2.19)–(2.21). This system of equations admits a number of useful analytical results for the case of $u_e = 0$ (from Maxworthy) or u_e constant. When $u_e = 0$,

$$\frac{U_v}{U_{v0}} = \left(1 + \frac{6\alpha U_{v0}t}{R_0}\right)^{-5/6}, \tag{2.23}$$

which on integration gives

$$\frac{X_v}{R_0} = \frac{1}{\alpha} \left(\left(1 + \frac{6\alpha U_{v0}t}{R_0}\right)^{1/6} - 1 \right). \tag{2.24}$$

For a field of turbulence maintained at a constant turbulent intensity u_0 , the penetration distance can be evaluated from

$$X_{max} = \int_{U_v}^0 \frac{dU_v}{\frac{dU_v}{dt} \frac{dX_v}{dX_v}} = \frac{R_0}{5\alpha} \left(\frac{\alpha}{\alpha_e I_t}\right)^{1/5} \int_0^{\alpha/\alpha_e I_t} \frac{d\tilde{U}}{\tilde{U}^{1/5}(1 + \tilde{U})}. \tag{2.25}$$

When $\alpha_e I_t/\alpha \gg 1$,

$$\frac{X_{max}}{R_0} \sim \frac{1}{4\alpha_e I_t} \left(1 - \frac{4}{9} \frac{\alpha}{\alpha_e I_t}\right). \tag{2.26}$$

The vortex model, based on the enhancement of boundary movement caused by entrainment, predicts a maximum penetration distance that varies inversely with I_t . Arnold *et al.* (2013) developed a ballistic model, based on large-scale vortices leading to differential advection of the vortex, with the maximum penetration distance scaling as $X_{max}/R_0 \sim 1/((L/R)I_t)$.

3. Numerical approach

The three-dimensional numerical component of the study examines the movement of an idealised vortex moving into a turbulent field. There are a number of choices for both the idealised vortex form (including a thin-cored vortex ring, Hill's spherical vortex) and turbulent field (forced or decaying homogeneous turbulence). In this paper, a Hill's spherical vortex (with $Re_0 = 2000$) moving into a decaying homogeneous turbulence is chosen. Other studies have initialised the flow with a Hill's spherical vortex (e.g. Camassa *et al.* 2013), but at lower Reynolds numbers (30–300).

3.1. Problem definition

A Hill's (1894) spherical vortex, with an initial radius R_0 and speed U_{v0} , moves into homogeneous turbulence, characterised by an initial root-mean-square (r.m.s.)-velocity u_0 and integral length scale L . The incompressible flow evolves according to the Navier–Stokes equation and the differential form of the conservation of mass, or

$$\rho \left(\frac{\partial \mathbf{u}}{\partial t} + \mathbf{u} \cdot \nabla \mathbf{u} \right) = -\nabla p + \mu \nabla^2 \mathbf{u}, \quad \nabla \cdot \mathbf{u} = 0. \quad (3.1a,b)$$

The fluid has a density ρ and dynamic viscosity μ . It is pertinent to evaluate the properties of a vortex evolving in time. Since the vortex moves through turbulence, the use of vorticity to discriminate the vortex edge, commonly applied to discriminate interfaces that separate turbulent from non-turbulent regions (see da Silva *et al.* 2014) is not viable. Experimentally, interfaces are typically discriminated using a passive dye represented as a scalar $C(\mathbf{x}, t)$ whose evolution in time is described by

$$\frac{\partial C}{\partial t} + \nabla \cdot (\mathbf{u}C) = D \nabla^2 C, \quad (3.2)$$

where D is the diffusivity of the scalar. In experimental studies with water, the diffusivity of dyes are 3 orders of magnitude smaller than the kinematic viscosity; the computational challenge of dealing with high Schmidt numbers generally precludes using scalars as a diagnostic to analyse vortex movement. An alternative approach is to use a Lagrangian method where fluid particles are tracked in time. A fluid particle located at \mathbf{X}_0 at $t = 0$ moves to \mathbf{X} in time t , where

$$\frac{d\mathbf{X}}{dt} = \mathbf{u}(\mathbf{X}, t), \quad \mathbf{X}(0) = \mathbf{X}_0, \quad (3.3a,b)$$

and this has the advantage of enabling the fluid exchange between the vortex and external flow to be assessed.

3.2. Flow initialisation

The initial flow $\mathbf{u}(\mathbf{x}, 0) = \mathbf{u}_v + \mathbf{u}_t$ is created by the superposition of a spherical vortex (\mathbf{u}_v) and a homogeneous turbulent field (\mathbf{u}_t) defined in a region starting a normal distance X_f from the vortex centre. The flow generated by the Hill's spherical vortex (Hill 1894),

Penetration of a spherical vortex into turbulence

$\mathbf{u}_v = (u_r, u_\theta)$ is set internally by

$$(u_{vr}, u_{v\theta}) = U_{v0} \left(\left(\frac{5}{2} - \frac{3}{2} \frac{r^2}{R_0^2} \right) \cos \theta, \left(-\frac{5}{2} + \frac{3r^2}{R_0^2} \right) \sin \theta \right), \quad (3.4)$$

where $r = |\mathbf{x}|$, $\theta = \cos^{-1}(\mathbf{x} \cdot \hat{\mathbf{x}}/r)$ and the internal azimuthal vorticity field is

$$\omega_{v\phi} = \frac{15U_{v0}}{2R_0^2} r \sin \theta. \quad (3.5)$$

Outside the vortex, the flow is described by

$$(u_{vr}, u_{v\theta}) = U_{v0} \left(\frac{R_0^3}{r^3} \cos \theta, \frac{R_0^3}{2r^3} \sin \theta \right), \quad (3.6)$$

and corresponds to the irrotational flow past a sphere. The Eulerian impulse and moment of the vortex are

$$I_{v0}^{(E)} = (1 + C_m)U_{v0}V_0, \quad M_{v0}^{(E)} = U_{v0}V_0, \quad (3.7a,b)$$

respectively, where $V_0 = 4\pi R_0^3/3$ and C_m and the added-mass coefficient takes a value of $1/2$.

An incompressible homogeneous random flow is constructed by a summation of Fourier modes chosen to satisfy a specified energy spectrum $E(k)$ (see Kraichnan 1959; Fung *et al.* 1992). The turbulent field is defined to start a distance X_f in front of the vortex centre so that it does not interfere with the initial stability of the vortex. This standard technique is based on an incompressible velocity field of the form

$$\mathbf{u}_t(\mathbf{x}) = \sum_{n=1}^{N_m} \mathbf{a}_n \times \hat{\mathbf{k}}_n \cos(\mathbf{k}_n \cdot \mathbf{x} + \phi_n) H(x - X_f), \quad (3.8)$$

where ϕ_n is a random phase, \mathbf{k}_n is a wavenumber vector, $\hat{\mathbf{k}}_n$ is a unit vector with random direction and \mathbf{a}_n is chosen so that the velocity field has the statistical properties of a prescribed energy spectrum $E(k)$. A range of wavenumbers is chosen to span the spectrum. Here, we set $N_m = 300$ and wavenumbers $k = k_n$ range from $0.2k_0$ to $10k_0$ (where $k_0 = 2\pi/L$). The wave vectors $\mathbf{k}_n = k_n \hat{\mathbf{k}}_n$ and \mathbf{a}_n are chosen from a distribution that satisfies

$$\langle \mathbf{a}_n \rangle = \mathbf{0}, \quad \langle |\mathbf{a}_n|^2 \rangle = 2 \int_{k_n - \delta k/2}^{k_n + \delta k/2} E(k) dk. \quad (3.9a,b)$$

We follow Fung *et al.* (1992) and prescribe an energy spectrum of the form

$$E(k) = \frac{\gamma g_2 (k/k_0)^4}{(g_1 + (k/k_0)^2)^{17/6}} \frac{u_0^2}{k_0}, \quad k_0 = \frac{2\pi}{L}, \quad (3.10a,b)$$

where

$$g_1 = \frac{\pi \Gamma^2(5/6)}{\Gamma^2(1/3)}, \quad g_2 = \frac{55}{9} \frac{g_1^{5/6}}{\pi}. \quad (3.11a,b)$$

Here, γ is a correction factor caused by limiting the wavenumber range and Γ is the gamma function (Abramowitz & Stegun 1964). The vorticity field associated with (3.8) is

$$\boldsymbol{\omega}_t(\mathbf{x}) = \nabla \times \mathbf{u}_t = \sum_{n=1}^{N_m} \mathbf{a}_n k_n \sin(\mathbf{k}_n \cdot \mathbf{x} + \phi_n). \quad (3.12)$$

The initial r.m.s. speed, $u_{rms(0)}$, was evaluated from the initialised velocity field with the ratio $u_{rms(0)}/u_0$ varying from 0.975 to 1.02.

3.3. Numerical solution

Equations (3.1a,b), (3.2) were solved using OpenFOAMv1706, which is a general computational object orientated package to solve multiphysics problems with a finite-volume formulation.

To study the vortex–turbulence interaction, the domain size was chosen to be $30R_0 \times 8R_0 \times 8R_0$. The effect of flow boundedness is expected to have a $1/8^2$ effect on the mean vortex speed. The vortex is initialised at a distance of $3R_0$ from the inlet plane, with $X_f = 5R_0$. A uniform block mesh was used – a variety of sizes were tested and we settled for $1000 \times 260 \times 260$. Slip boundary conditions were applied to the walls of the domain and the simulations ran until time $\tilde{t}(= U_{v0}t/R_0) = 50$. Mesh convergence was tested by analysing the vortex position as a function of time and this showed less than 2 % difference in the vortex position between simulations running at 8.45 million cells compared with 67.6 million cells. The evolution of the r.m.s. speed of the homogeneous turbulence was calculated as a function of time and fitted with a power law of the form

$$\frac{u_e}{u_0} = \left(1 + \frac{2.0u_0t}{L} \right)^n, \quad (3.13)$$

with a decay index of $n = -0.7$, which is typical for decaying homogeneous turbulence (Wilczek, Daitche & Friedrich 2011).

The vortex centre, X_v , was calculated from the Lagrangian position of N_p fluid particles that were initially located within the vortex

$$X_v = \frac{1}{N_p} \sum_{i=1}^{N_p} X_i. \quad (3.14)$$

Since the fluid particles are advected by the local fluid velocity (see (3.3a,b)), the vortex velocity is

$$U_v = \frac{1}{N_p} \sum_{i=1}^{N_p} \frac{dX_i}{dt} = \frac{M_x^{(L)}}{V_0}. \quad (3.15)$$

The vortex radius was defined in terms of the standard deviation from the vortex centre, so that $R_{std} = \overline{(X_i - X_v)^2}^{1/2}$. The vortex was seeded with $N_p = 10^4$ particles.

4. Experimental set-up and measurements

In the laboratory, the interaction of a vortex with turbulence is studied in a cubic Plexiglas tank of $1.0 \times 1.0 \times 0.90 \text{ m}^3$ filled with tap water to a height 89 cm, as shown in figure 3(a). Approximately thirty minutes prior to the vortex generation near the fluid surface, the

Penetration of a spherical vortex into turbulence

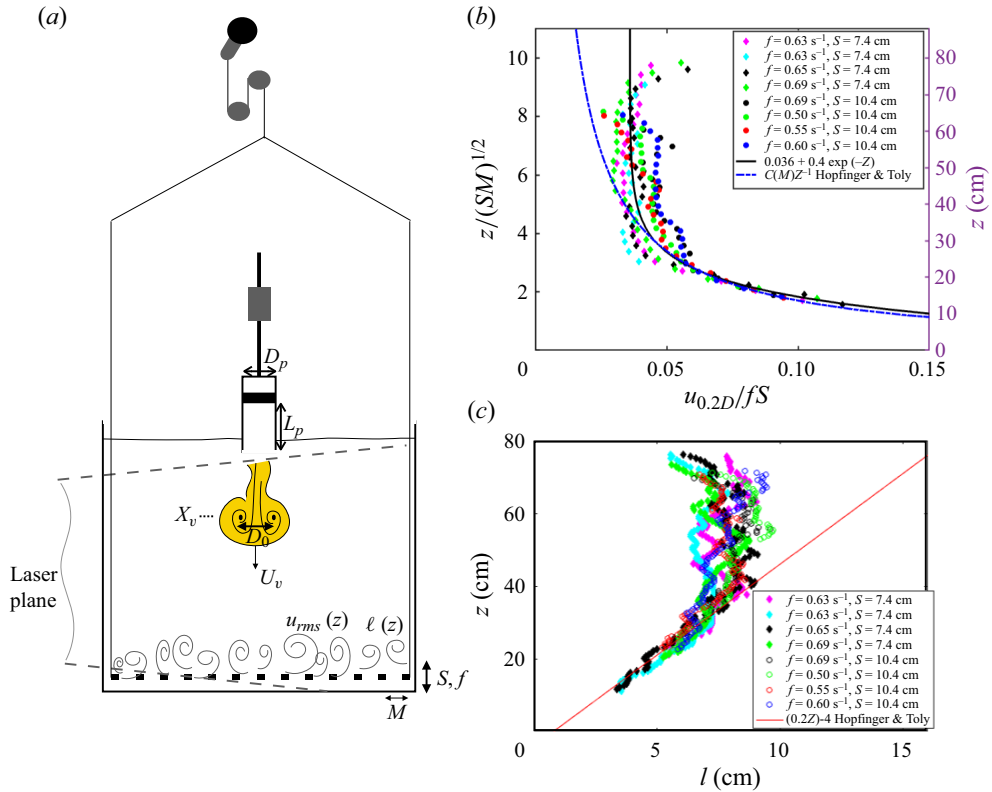


Figure 3. (a) Schematic of the experimental set-up, showing the piston dimensions (diameter D_p , stroke length L_p) and grid dimensions (stroke distance S and bar separation M). The grid mass was increased with metal weights (not shown) to stabilise its motion. The box turbulence is characterised in terms of (b) the scaled turbulent velocity, u_{rms}/fS , fitted with an exponential $a + b \exp(-cz)$, (see legend and (4.3)) and (c) turbulent length scale, l , plotted against height z above the grid. The origin $z = 0$ corresponds to the maximum height of the grid (see Hopfinger & Toly 1976), i.e. ≈ 5 cm above the bottom of the tank.

turbulence generation is started near the bottom of the tank by the vertical (and sinusoidal) oscillation of a grid with a mesh size close to that used in Hopfinger & Toly (1976). To visualise the flow, the fluid is seeded with spherical particles with a diameter of $60 \mu\text{m}$ and density of approximately $\rho = 1.03 \text{ g cm}^{-3}$, while the vortex is coloured with a fluorescent dye (Rhodamine 6G). A small amount of sodium hydrochlorate is added to the water in order to slowly bleach the dye and to be able to repeat the experiment in the same fluid. The flow is illuminated by a vertical laser sheet passing through the centre of the tank, generated with a 2 W Spectra Physics Millennia Pro laser and cylindrical lens. For the recording and flow measurements a Dalsa 1M60 Pantera camera is used with a frame rate between 5 and 20 Hz (see figure 3) and a Sony Alpha III camera. These recordings are processed with the particle image processing program UVmat (<http://servforge.legi.grenoble-inp.fr/projects/soft-uvmat>), developed at LEGI, which allowed for the measurements of the r.m.s. velocity of the turbulence as well as the vorticity fields, whereas the dye visualisations are processed with ImageJ (<https://imagej.net/>). The distance of the vortex centre from its start, X_v , and vortex radius, R_v , defined in terms of the separation of the vortex cores, are determined from vorticity maxima and dye visualisation, as functions of time. The vortex speed, U_v , is deduced from the displacement of the

Exp. Label	f (Hz)	S (cm)	D_p (cm)	U_{v0} (cm s ⁻¹)	D_0 (cm)	$\bar{u}_{0,2D}$ (cm s ⁻¹)	X_{max}/R_0	$U_{v0}/\bar{u}_{0,2D}$
A	0.63	5.4	4	2.778	5.358	0.123	12.971	22.548
B	0.63	5.4	4	3.083	6.222	0.154	14.588	19.974
C	0.65	5.4	4	4.128	5.915	0.168	13.665	24.548
D	0.65	7.4	4	1.553	6.250	0.173	4.599	8.960
E	0.65	7.4	4	9.279	5.967	0.193	19.639	48.082
F	0.65	7.4	4	9.346	6.603	0.219	18.541	42.652
G	0.65	7.4	4	7.546	6.029	0.193	16.862	39.024
H	0.5	5.4	11	2.203	14.550	0.120	9.138	18.312
I	0.625	5.4	11	2.103	14.847	0.131	7.761	16.041
J	0.625	5.4	11	2.180	14.605	0.139	8.651	15.705
K	0.625	5.4	11	3.283	14.725	0.155	9.177	21.206
L	0.65	10.4	11	3.235	17.485	0.311	4.494	10.395
M	0.67	10.4	11	1.408	14.732	0.252	1.212	5.583
N	0.50	10.4	11	1.232	14.337	0.189	2.379	6.510
O	0.55	10.4	11	1.320	11.827	0.212	4.264	6.219
P	0.55	10.4	11	1.452	11.041	0.210	4.448	6.918
Q	0.60	10.4	11	0.528	14.094	0.226	1.117	2.335
R	0.60	10.4	11	0.264	13.525	0.226	0.484	1.170
S	0.60	10.4	11	1.056	11.833	0.226	1.544	4.674
T	0.65	7.4	11	2.219	14.537	0.198	6.034	11.206

Table 1. Data of the vortex in oscillating grid turbulence. The parameters f , S , D_p and D_0 (which is $\approx 2R_0$) are defined in figure 3(a); U_{v0} and $\bar{u}_{0,2D}$ are the vortex and r.m.s. in-plane turbulent velocities at $t = 0$, respectively, whereas X_{max}/R_0 is the scaled maximum travelled distance by the vortex. The vortex starts in turbulence so that $X_f = 0$.

vortex centres. The turbulence of the grid is calibrated, such that the turbulent velocity, u_e , and length scale ℓ , are known from the forcing parameters.

The vortices are injected a few centimetres below the tank free surface, at approximately $z = 84$ cm, such that the vortex centres of the formed vortex are at approximately $z = 73$ cm above the virtual origin in figure 3(b,c). The translation velocity U_v of the vortex is measured from the dye and, for some cases, verified with the displacement of the vorticity maxima from particle image velocimetry (PIV) measurements. Below the details of the vortex generation and turbulence generation are discussed.

4.1. Vortex generation

The vortex was generated by the movement of a piston, controlled by a stepper motor, which drives flow through a pipe with internal diameter $D_p = 11$ cm or $D_p = 4$ cm. The initial speed of this vortex, U_{v0} , is proportional to the piston velocity, whereas the circulation is determined by the distance travelled by the piston, and the size of the vortex is mainly determined by the diameter of the cylinder (see Gharib, Rambod & Shariff 1998, for details). The displacement distance of the piston to generate the vortex ring, L_p , was kept constant and equal to 13.65 cm during each experiment, so that the vortex formation number, L_p/D_p , was fixed at a value of 1.24, and 3.41 in the case of the small vortex. Since this vortex formation number is below 4 in this study, only isolated vortex rings were generated with no (or hardly any) trailing wake (e.g. Gharib *et al.* 1998). The Reynolds number of the vortex, based on the initial velocity U_{v0} and diameter D_0 just after generation, $Re_0 = D_0 U_{v0}/\nu$, was varied between 1490 and 5660 (see table 1).

4.2. Turbulence generation and properties

A turbulent field is generated with a vertically oscillating grid, made of square bars of thickness $d = 1.5$ cm, separation $M = 6$ cm covering an area 97 cm \times 97 cm. The gap between the grid and the sidewall of the tank is minimised with 5 mm thick matt black Perspex plates. This also improves the quality of the recordings. The stroke of the grid, S , was varied at the values 5.4 , 7.4 and 10.4 cm.

The characteristics of the turbulence are set by the grid forcing frequency (f) and amplitude of forcing (S), with the characteristic velocity and length scale set by the grid. Turbulence statistics are obtained from long time statistics of planar PIV measurements in a vertical plane. The in-plane r.m.s. velocity $u_{0,2D}$ and integral length scale L are expressed in terms of the in-plane velocity fluctuation, u' , through

$$u_{0,2D} = \overline{(u'^2)}^{1/2}, \tag{4.1}$$

and

$$L = \int_0^{R_L} \overline{u'(r)u'(r+x)} \, dr / \overline{(u'^2)}, \tag{4.2}$$

where R_L is the upper bound for the correlation integral. The results for $u_{0,2D}$ and L are shown in figure 3(b,c) as a function of distance z . At larger distances from the grid, where the small structures between the plumes that are generated by the moving bars are dissipated, the turbulence intensity and integral length scale tends to a constant. Similar results of a constant $u_{0,2D}$ and length scale L were also obtained for faster grid motion ($f \sim 1$ Hz) and a smaller stroke S (personal communication with J. Sommeria). Close to the moving grid, the turbulent intensity increases and the integral scale decreases as the flow is dominated by the shedding of small intense vortices from the grid. In view of the present interest of knowing the turbulence intensity at a particular level, an exponential fit was employed

$$\frac{u_{0,2D}}{fS} = 0.036 + 0.4 \exp\left(-\frac{z}{(SM)^{1/2}}\right), \tag{4.3}$$

which is shown in figure 3(b). The saturation of the turbulence near a constant value of u_{rms} and L has not been observed in Hopfinger & Toly (1976) and more recently Poulain-Zarcos, Mercier & Halle (2022) since, in these experiments, the measurement region is limited to a distance of 35 cm of the grid position. In Hopfinger & Toly (1976) the grid oscillated at mid-depth in a 80 cm height tank with a ten times faster oscillation frequency, leaving an effective 35 cm distance from the grid, as also in Poulain-Zarcos *et al.* (2022). Further, a ten times lower frequency was used to keep the turbulence weak compared with the vortex. Figures 3(b) and 3(c) show indeed that, at $z > 30$ cm, the length scale L stagnates around a value of $\approx 7.5 \pm 1.5$ cm, corresponding to the mesh size, while $u_{0,2D}/fS^{3/2} \approx 0.013$, implying a maximum Reynolds number of $Re_t = u_{0,2D}L/\nu$ roughly between 120 and 240 .

In Hopfinger & Toly (1976), the grid oscillated at the tank mid-height, and the virtual origin (where $L = 0$) corresponded to the position $z_{top} - (S/2 + 0.01m)$, with z_{top} the maximum position of the grid, thus slightly below centre position of the grid. This is also taken as the reference position ($z = 0$) in figure 3(b,c). In the present experiments, the grid oscillates near the bottom and the level with $L = 0$ corresponding to the bottom of the tank, showing the effects of a nearby boundary on the turbulence.

The turbulent intensity in the vicinity of the vortex changes as the vortex descends. To compare the experimental results with the numerical simulations, a consistent definition

of the turbulent intensity is taken

$$I_t = \frac{(3/2)^{1/2} \bar{u}_{0,2D}}{U_{v0}}, \quad (4.4)$$

that is expressed in terms of $\bar{u}_{0,2D}$ and determined by averaging $u_{0,2D}$ over the path of the vortex. The prefactor $(3/2)^{1/2}$ is used to convert the in-plane r.m.s. velocity to the r.m.s. of the three-dimensional velocity field.

5. Numerical results: vortex movement into a quiescent region

5.1. Vortex-induced transport

To distinguish between the effect of the vortex on transport outside the vortex from the processes that occur within the vortex, two groups of fluid particles were followed in time – see figure 4. Drift is associated with differential movement of fluid and was quantified using a distribution of particles in the plane $z = 0$ in the form of a structured grid. The lateral displacement of the grid lines parallel to the direction of vortex propagation gives an indication of blocking and source strength, while the distortion of the grid lines perpendicular to the vortex propagation indicates Darwin drift. To characterise the transport by the vortex fluid particles are seeded randomly within the vortex and followed in time. The two groups of fluid particles are distinguished by colour (see figure 4a), with those initially inside the vortex being blue and those initially outside the vortex being red.

The drift profiles confirm the longitudinal displacement profiles reminiscent of those identified by Darwin and Maxwell. Drift profiles have been used to analyse the kinematic transport by dipolar vortices (Eames & Flor 1998). The stretching of fluid elements passing close to the stagnation points is clear, leading to a tilting of fluid elements along the x -axis. The lines of fluid particles parallel to the propagation direction are laterally displaced, as a consequence of the volume flux deficit behind the vortex. The lateral divergence is a consequence of the presence of the source flow due to the drag on the vortex. The lateral displacement behind the vortex is approximately constant over the period of these simulations. The volume flux behind the vortex changes when the manner in which the vorticity is deposited in the wake is interrupted and this is observed to occur when the vortex is undergoing an inviscid adjustment, corresponding to a time beyond $\tilde{t} = 40$. Consequently, the drag on the vortex is approximately constant up until this time. In the external flow around the vortex, the accumulation and stretching of fluid particles near the leading stagnation point highlights the front of the vortex. Their motion confirms that the fluid enters the rear of the vortex and circulates in the vortex core. At a later time ($\tilde{t} \sim 40$), the edge of the vortex is difficult to distinguish from the side view due to three-dimensionality of the flow. The non-uniform radial particle distribution within the vortex indicates the entrainment of ambient fluid which does not contain particles.

5.2. Velocity and vorticity field

Hill's spherical vortex is based on a steady inviscid model where the initial strength of ω_ϕ varies linearly with distance from the centreline (see (3.5)). The most significant process is the loss of vorticity due to the diffusive flux across the bounding streamline, which leads to vorticity being deposited behind the vortex. It is this loss which leads to a faster reduction of the maximum vorticity in the vortex than vorticity annihilation. The width of the vortical wake behind the vortex is βR_0 (where $\beta \sim 1/3$) is smaller than for a solid body because of the absence of flow separation that arises from the no-slip

Penetration of a spherical vortex into turbulence

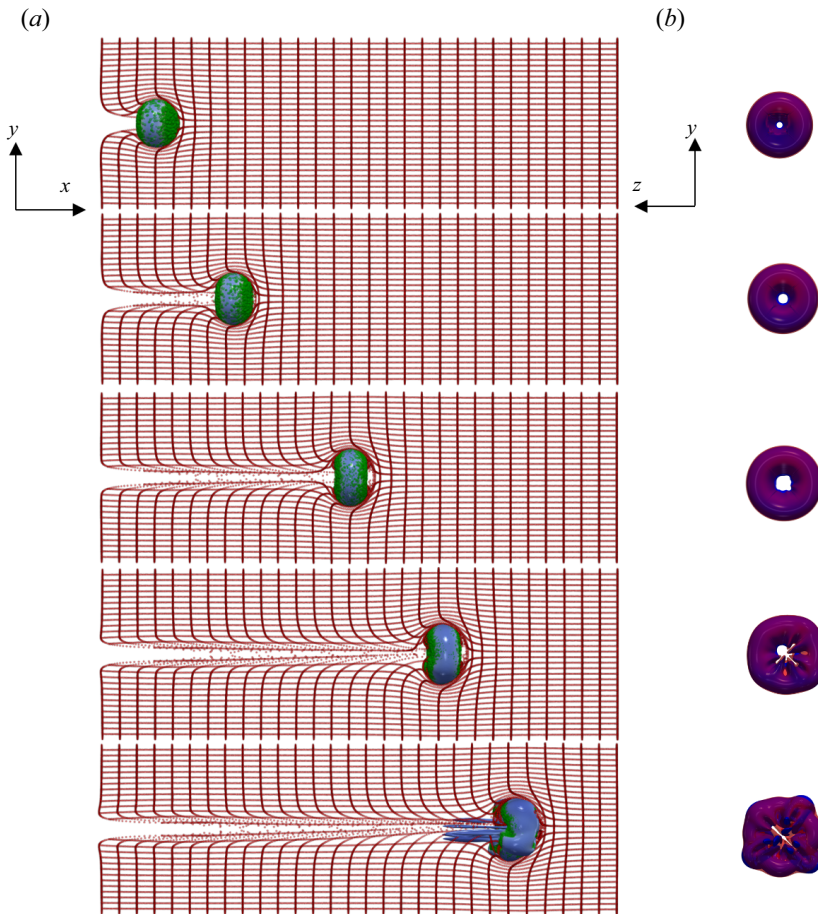


Figure 4. (a) Time sequence showing the displacement and transport of fluid particles by a Hill's spherical vortex moving with initial Reynolds number $Re_0 = 2000$. The red particles were initially placed in a grid arrangement with planes that lie perpendicular and parallel to the initial velocity of the vortex; the green particles were placed randomly within the vortex. The panels are shown for $\tilde{t} = 5, 10, 20, 30$ and 40 where $\tilde{t} = U_{v0}t/R_0$. The vortex is represented as an iso-surface of the second invariant of the velocity gradient tensor, $II = \frac{1}{2}(\|\boldsymbol{\Omega}\|^2 - \|\mathcal{S}\|^2)$, where $\boldsymbol{\Omega} = (\nabla\mathbf{u} - (\nabla\mathbf{u})^T)/2$ and $\mathcal{S} = (\nabla\mathbf{u} + (\nabla\mathbf{u})^T)/2$ (Hunt, Wray & Moin 1988). The iso-surface $II = 0.02 \text{ s}^{-2}$ is plotted. (b) The projected view of vortex shown iso-contour of $II = 0.02 \text{ s}^{-2}$ and $|\boldsymbol{\omega}| = 0.1 \text{ s}^{-1}$.

condition; the vorticity strength on the surface of the solid body scales as $U_0/R_0Re^{1/2}$. The vortex wake is much larger than a clean spherical bubble (Moore 1963), even though the vortical strength is comparable (U_0/R_0), because of the kinematic constraint imposed by the bubble surface. The width of the downstream vortex wake is largely determined by cross-stream diffusion in a negatively strained flow, which tends to greatly widen the wake (Hunt & Eames 2002). Viscous diffusion of oppositely signed vorticity on the centreline of the vortex leads to vorticity annihilation. This effect is far weaker than Maxworthy identified because vortex compression leads to ω_ϕ tending to zero on the centreline. At a later time of $\tilde{t} = 40$, the azimuthal instability has grown sufficiently large that the vortex starts to become asymmetric. This instability is likely due to the mechanism explained by Widnall (Widnall & Sullivan 1973) and appears for $Re \gtrsim 2000$ (see Maxworthy 1977).

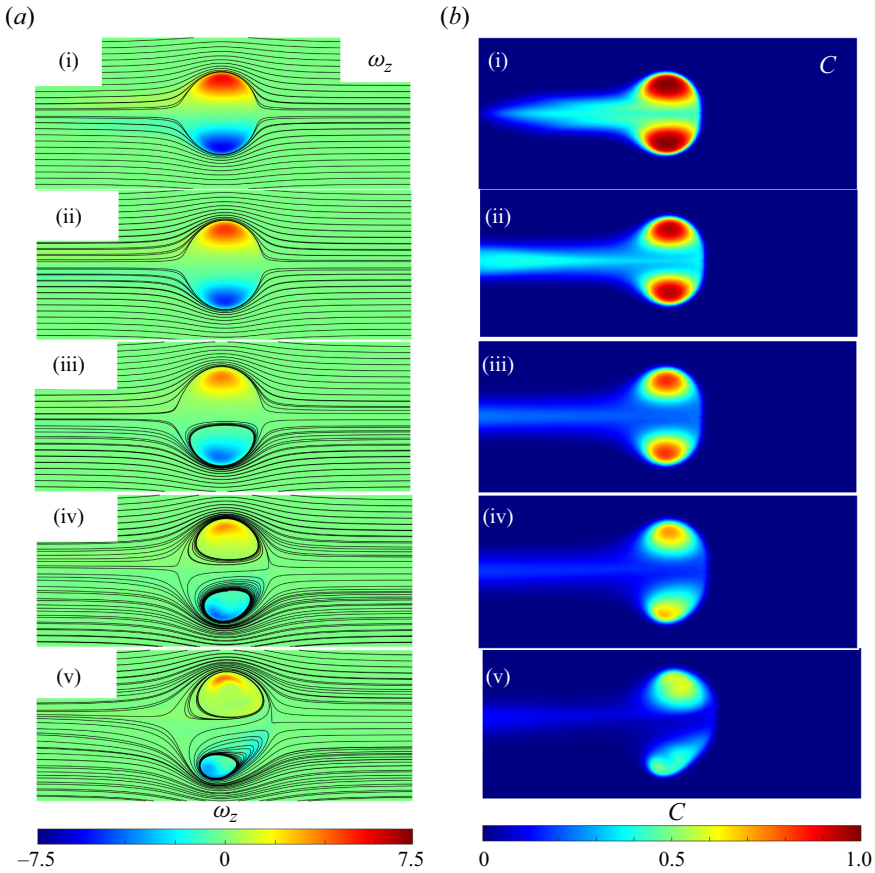


Figure 5. (a) The distribution of vorticity ω_z in the plane $z = 0$, is shown for $\tilde{t} = 5, 10, 20, 30$ and 40 . The streamlines are plotted in the frame moving with the vortex, where the vortex speed is determined from the average Lagrangian velocity. (b) The distribution of scalar, C , initially set as $C = 1$ within the vortex, is indicated for times $\tilde{t} = 5, 10, 20, 30$ and 40 .

The planar streamline pattern, in the frame moving with the vortex, is shown in figure 5(a), along with the distribution of the vorticity component that is normal to the page. The vortex centre and velocity are determined from the fluid particles initially released inside the vortex. The permanent cross-stream displacement of streamlines originating upstream of the vortex, seen in figure 5(a), are indicative of a source flow, or equivalently, a drag on the vortex.

As the vortex propagates, the vortex core changes shape and material is shed into its wake. Cross-stream slices of the scalar distribution are shown in figure 5(b i–v). Material is lost from the vortex through a diffusive flux at the side of the vortex (see figure 5a) with a trail of vorticity and tracer in the wake. The diffusivity of the tracer is set the same as that of vorticity. The overall growth of the three-dimensional effects is affected by both mesh resolution and mesh shape.

5.3. Speed, shape and impulse

The vortex position was calculated from the mean and the maximum distance moved by marked internal fluid particles and both gave substantially the same result, as shown in figure 6(a). Figure 6(a) shows a comparison with the model and $\alpha = 0.012$. This agrees

Penetration of a spherical vortex into turbulence

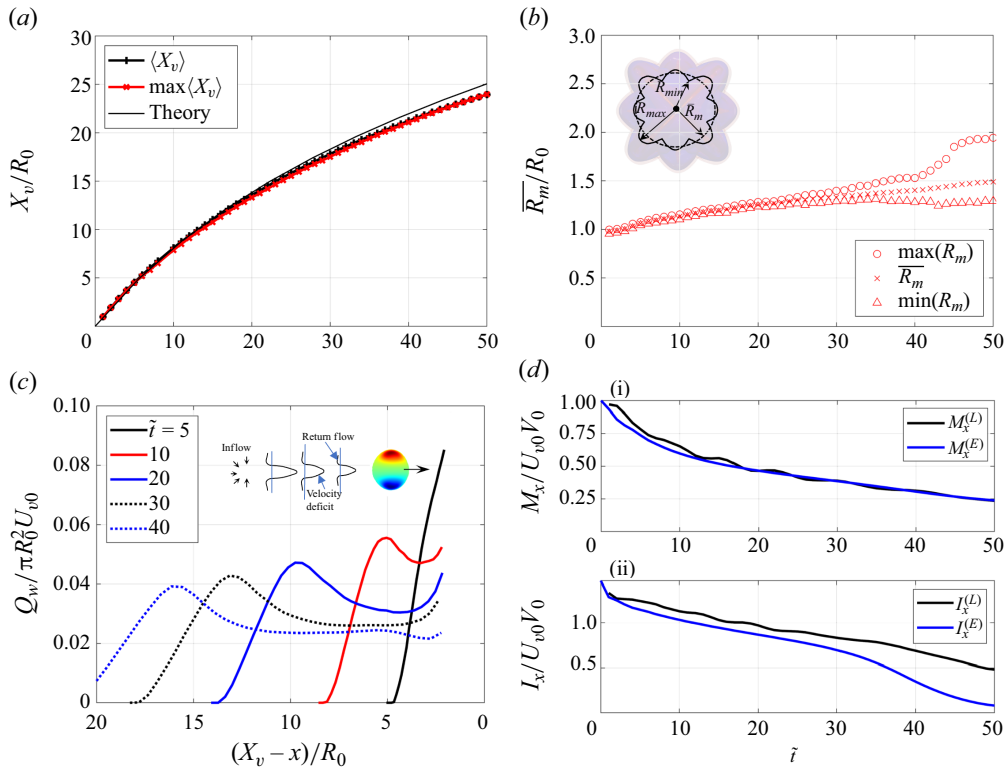


Figure 6. (a) The vortex position, X_v , determined from Lagrangian particle information, is plotted as a function of time (see legends for symbols). (b) Characterisation of the cross-sectional shape of the vortex (determined from the maximum radial distance $R_m(\theta)$ mean and minimum of R_m of Lagrangian particles from the centreline). (c) Volume flux Q_w , determined from (2.8) as a function of distance behind the vortex, for different times (see inset). (d) Scaled Lagrangian and Eulerian measures of momentum (M_x) and impulse (I_x) as functions of time.

for short time during which the three-dimensional deformation of the vortex ring is still small, since, from figure 6(c), $C_Q = Q_w/\pi R_0^2 U_{v0} \sim 0.10$, giving $\alpha \sim 0.0125$. At around $\tilde{t} \sim 40$, the azimuthal instability mentioned above starts to grow and the simple drag model is not applicable. The vortex decreases faster than anticipated, apparently due to the rapid increase in its radius.

To explore the adjustment from an axisymmetric vortex ring to a ring with a series of modes, the shape of the vortex was analysed using information from the Lagrangian particles. Projecting the particles onto a normal plane enabled the outer edge of the vortex $R_m(\theta)$ to be determined (see figure 6(b) inset), from which the average (\bar{R}_m), maximum and minimum ($\max(R_m)$, $\min(R_m)$) are determined. We would speculate, based on Maxworthy's (1977) observations, that the vortex will ultimately break down.

The volume flux Q_w , downstream of the vortex, is evaluated from (2.8) as a function of distance from the vortex centre, and shown in figure 6(c) for four times. During the initial movement of the vortex, the diffusive flux of vorticity into the wake tends to occur at a constant rate, giving rise to a constant volume flux, except beyond the starting point where the flow is irrotational. The volume flux behind the vortex starts to decrease at around $\tilde{t} = 20$, as the inviscid adjustment causes the size to increase and the vortex entrainment becomes pronounced. This is also evident in figure 5(b), where the tracer concentration in the near wake is also diminished.

6. Vortex moving into a region of turbulence

6.1. Numerical results

Figure 7(a) shows the movement of the initially spherical vortex, for different background levels of turbulence ($I_t = 0.1, 0.2$ and 0.5). The vortex is visualised by placing fluid particles within the vortex and following their evolution in time. The vortex is initially compact in the non-turbulent region and then quickly loses mass through the wake as it moves into the region of turbulence. With increasing strength of external turbulence, the rate at which the vortex loses mass increases. Its head remains initially coherent and, while the tagged fluid elements tend to be dispersed in the longitudinal direction, the size of the head of the vortex increases more slowly. At a later stage, the growth of the vortex tends to be dominated by passive dispersion. The presence of turbulence leads to the vortex tending to slow down with an increased sensitivity to being deflected by the ambient turbulence. The mutual distance between the vortices increases while they deform, and flatten the more they enter in the turbulent region. With higher levels of turbulence, the vortex is blocked over a shorter distance and deforms faster, so that the penetration distance decreases. These effects become more pronounced with the intensity of the turbulence.

Figure 7(b) shows the vortex position as a function of time and indicates that, over the period of the tests, the vortex slows down faster as it penetrates into the turbulent region (figure 7c i). At the higher values of turbulent intensity, the vortex is largely arrested and is observed to penetrate a finite distance into the turbulence. The impulse of the vortex decreases due to the loss of vorticity but it has a very specific tendency to increase as it interacts with the interface between the turbulent and non-turbulent region. This blocking effect is similar to a vortex impacting a wall which causes the vortex to flatten, vorticity to increase via stretching, leading to an increase in the vortex impulse (see Verzicco *et al.* 1995). This is evident in figure 7(c ii) for the highest external turbulence ($I_t = 0.5$). The change of vortex impulse due to vorticity diffusion is negative except for short periods with $I_t = 0.5$, when detrained fluid elements pick up vorticity from the ambient turbulence.

Figure 8 shows the turbulent field and vortex, as isocontours of Q , for different times and turbulent intensities. The colour in the images shows the (normalised) concentration of the scalar tracer and gives an indication of the material that was originally within the vortex. The decaying turbulence leads to an increase in the integral length scale and decrease in the r.m.s. velocity, which is seen by the increased space between vortical tubes. The interface between the turbulent and non-turbulent region is deflected by the initial penetration into the turbulence, and eventually disperses. The sequences show that the coherence of the vortex is quickly lost as the strength of the external vorticity increases. The size of the vortex, evident from the highest concentration of passive scalar, grows in time. For the lowest level for turbulent intensity ($I_t = 0.1$), the shed material is concentrated along the vortex path and the wake vorticity quickly dispersed by the external turbulence.

The penetration of the vortex into homogeneous turbulence is thus accompanied by a reduction in the vortex speed associated with the loss of wake material and vortex growth in size. The vortex speed U_v is determined from the Lagrangian measure of momentum (M_x^L/V_0). For $I_t = 0.1$, the reduction of speed leads to an approximately linear decrease of velocity with distance with a rate faster than in the absence of turbulence (figure 9a). Both the ambient turbulence and the vortex speed decrease in time but at different rates; initially the ambient turbulence decreases faster than the vortex speed, leading to U_v/u_0 increasing, but since the loss of mass from the vortex is continuous, the vortex ultimately slows down faster than the rate at which the turbulence decays.

Penetration of a spherical vortex into turbulence

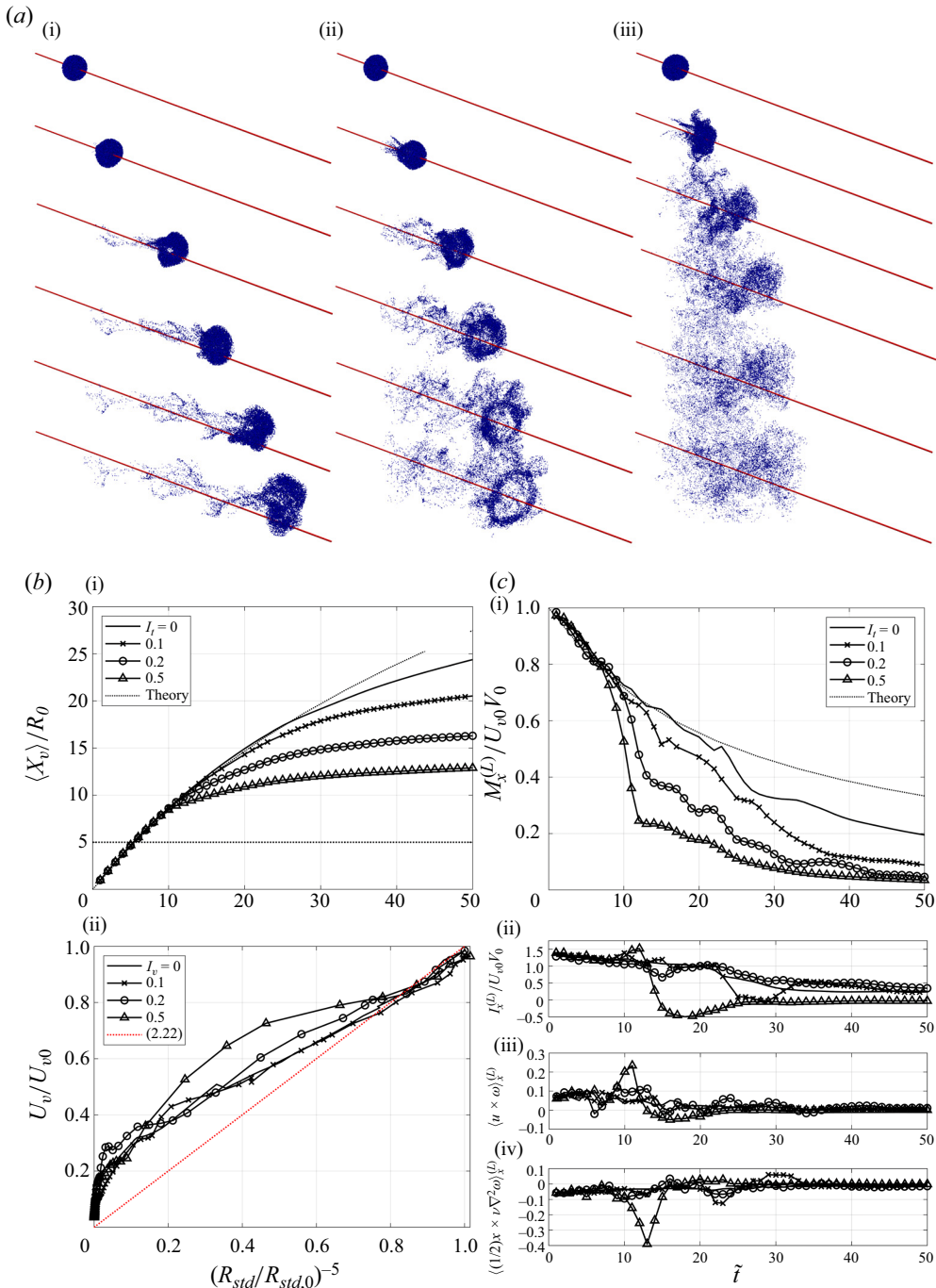


Figure 7. (a) Lagrangian transport of fluid particles by a vortex moving into a turbulent flow for contrasting levels of ambient turbulence (i) $I_t = 0.1$, (ii) 0.2 and (iii) 0.5; in each case $L/R_0 = 4$, at times $\tilde{t} = 5, 10, 20, 30, 40$ and 50. A red line is plotted along the centre of the domain, starting from the initial vortex position, to give perspective to the images. The position of the vortex is shown in (b i) and the normalised velocity plotted against the vortex radius in (b ii). A horizontal line is plotted at $X_f/R_0 = 5.0$. The decay of the vortex velocity is shown in (c i) for contrasting levels of turbulent intensity. The Lagrangian measures of vortex for (c i) momentum, (c ii) impulse, (c iii) vortex force and (c iv) diffusive flux of impulse are shown as functions of time.

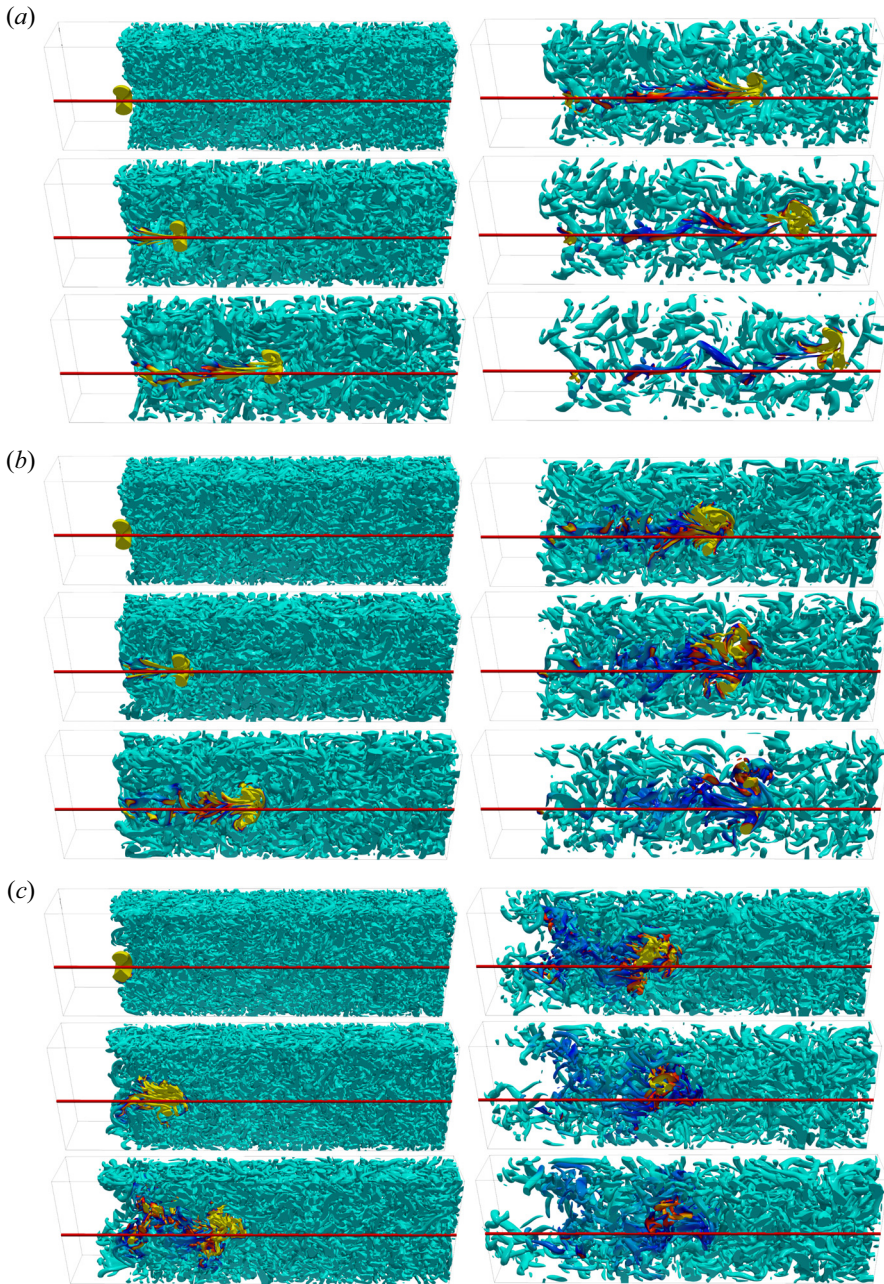


Figure 8. A cross-section of the flow structure is shown for (a) $I_t = 0.1$, (b) 0.2 and (c) 0.5. The iso-volume contours for the second invariant of the velocity gradient tensor Q are shown, with values $QR_0^2/U_{v_0}^2$ shown greater than 0.025, 0.0125 and 0.0005, respectively, for (a–c). The time instances correspond to those in figure 7(a). The colour field corresponds to the scalar field C and varies from cyan to yellow (from $C = 0$ to maximum C). The reference red line is the centreline of the simulations. The lateral span of the box indicates the vortex start and the end of the computational domain, which is smaller than the computational domain.

Penetration of a spherical vortex into turbulence

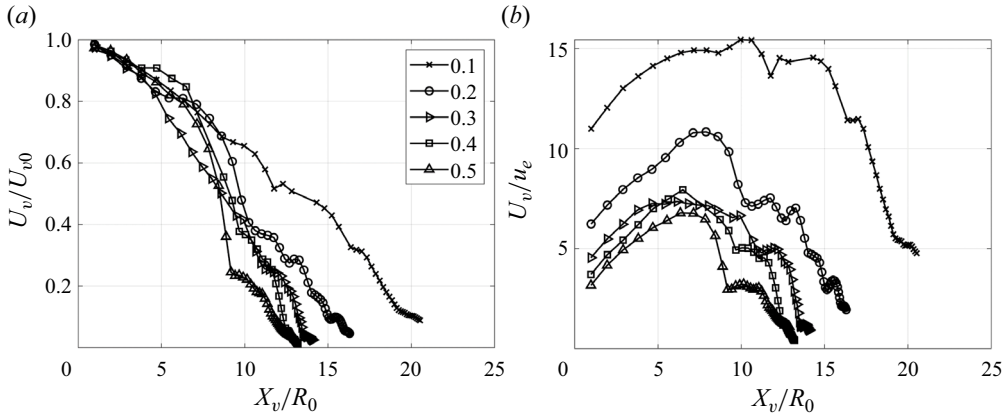


Figure 9. The vortex speed, U_v (3.15), determined from the numerical simulations, is shown as a function of the distance the vortex has moved. In (a), the contrasting influence of turbulent intensity is shown. In (b), the ratio of the U_v/u_e is shown as a function of vortex position, where u_e is determined from (3.13).

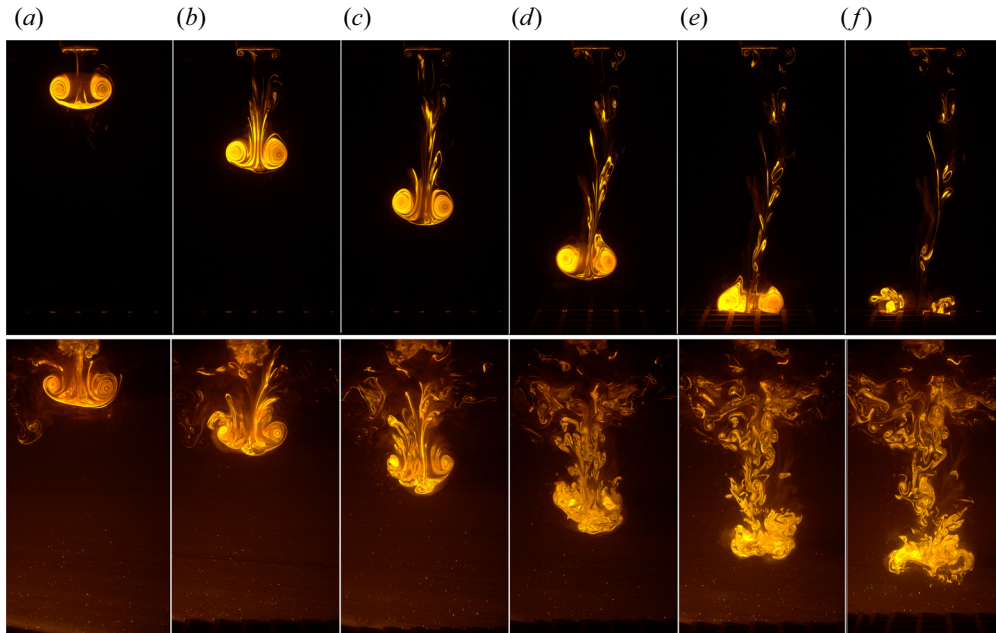


Figure 10. Typical vortex evolution in quiescent ambient fluid (top), and with ambient turbulence generated by an oscillating grid near the base of the tank (bottom) at (a) $t = 3.5$, (b) 10.8 (c) 17.2 (d) 24.7 (e) 30.9 and (f) 35.3 s after the vortex generation. The internal diameter of the cylinder is 11 cm (see experiment Q in table 1, and the same parameters for top images without turbulence). The frames are 50 cm wide, and the position of the grid is represented in (f) by the black area near the bottom.

6.2. Experimental results

Typical visualisations of the evolution of the vortex moving in quiescent fluid (top row) and in turbulence (bottom row) generated by the oscillating grid near the bottom of the tank are shown in figures 10(a)–10(f) for the vortex generated with the 11 cm (inner) diameter tube. Below we discuss the figures in the bottom row. During an initial stage, the

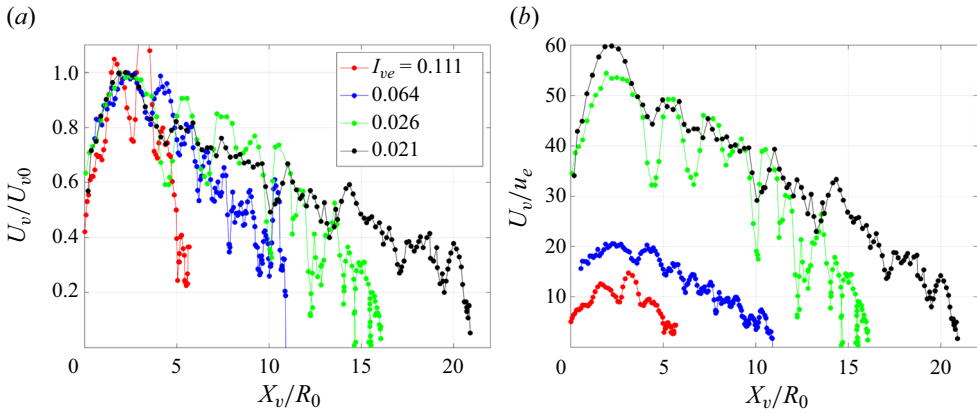


Figure 11. Results from the experimental study of (a) the vortex velocity U_v and (b) the normalised vortex velocity U_v/u_e , as a function of distance from vortex starting for contrasting values I_{ve} .

vortex develops and grows as a result of entrainment (see figure 10a), showing relatively little influence of the ambient turbulence for the large vortex. Small turbulent vortices in the ambient are advected around the spherical vortex, and either strained in the wake of the spherical vortex, or entrained into the spherical vortex, leading to its intensification (see figure 10b,c). During this latter process, the spherical vortex moves outwards causing the propagation velocity to decrease. As the vortex moves forward it confronts smaller but more intense turbulent vortices are confronted, leading to the breakup of the sharp vortex front into smaller vortices (see figure 10d–e). When the vortex approaches the top position of the grid (at approximately $z = 20$ cm), the vortex is eventually destroyed by the turbulent jets generated by the oscillating grid (see figure 10f). Although the same sequence was observed for the smaller vortices (generated with the 4 cm diameter tube), the turbulent vortices are now comparable to the size of the grid, which deviates, intensifies or weakens the initial vortex during its development stage, increasing the variance of the speed and size.

The position of the vortex centres, X_v , are determined by manual segmentation of images, such as figure 10, and also from the vorticity extremes obtained from PIV measurements. Following the dye that is captured in the vortex centres, the vortex velocity was then calculated by differentiating X_v with time. The turbulence intensity at the vortex centre is obtained by interpolating the u_0 relation shown in figure 3(b). The initial position of the vortex, X_{fe} , is considered as the moment the vortex was formed. The vortex radius, R_0 , is measured shortly after injection as half the distance between the two vortex centres when it has reached its mature state, i.e. it has a circular shape and slightly increases in speed. In case this is not possible because the vortex was perturbed by ambient vortices, its maximum velocity shortly after injection has been taken.

Figure 11 shows the evolution of the vortex velocity with penetration distance. The oscillations in U_v/U_{v0} and U_v/u_e are due to the small turbulent vortex structures that are advected to the rear of the spherical vortex where they are entrained. Subsequently, these small-scale vortices are swept internally to the front of the vortex. During this entrainment process the spherical vortex slightly expands in size, and by conservation of impulse, decreases in speed (figure 11a). Figure 11(b) shows the relative strength of the vortex to the local turbulent intensity, which decreases rapidly with distance; by comparing figures 9(b) and 11(b), the vortex appears to be arrested when $U_v/u_e \sim 2-5$.

Penetration of a spherical vortex into turbulence

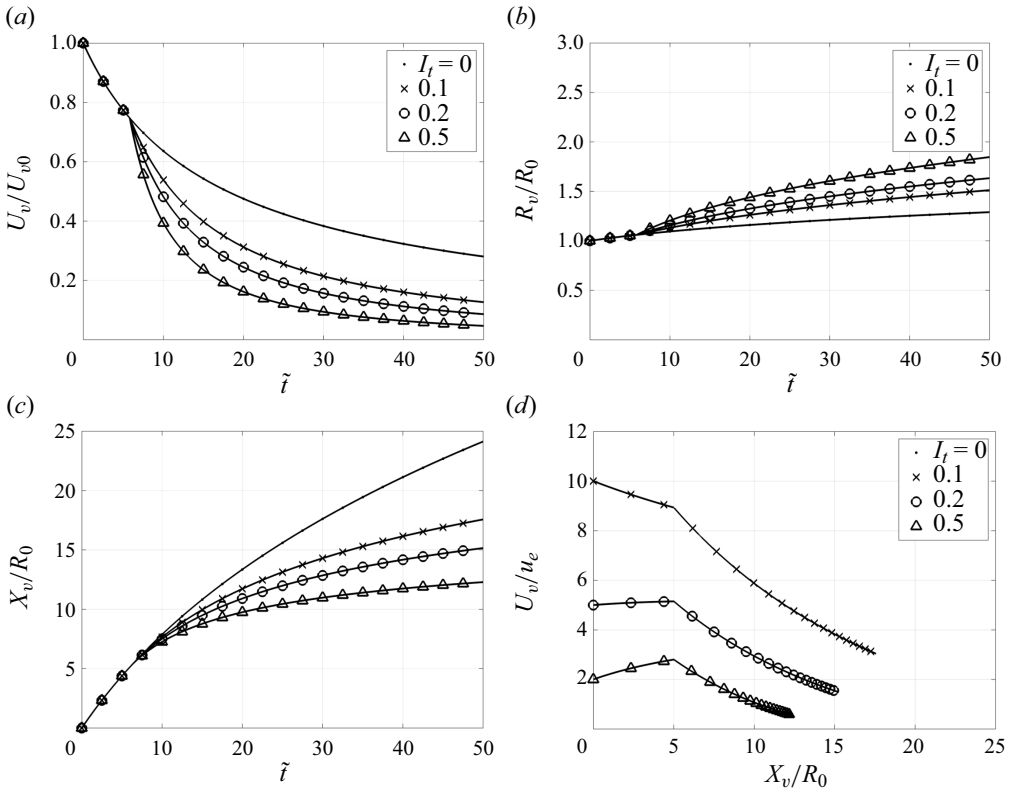


Figure 12. Predictions for the vortex dynamics based on the integral model (2.19)–(2.20) for (a) radius, (b) velocity and (c) position with time, and (d) speed with vortex position, where the turbulence decays according to (3.13) for $n = -0.7$.

6.3. Comparison of numerical, experimental and integral models

The numerical model is based on decaying, homogeneous turbulence and contrasts with the box turbulence in the experimental study, which is statistically steady but spatially varying. The integral model (2.19)–(2.21) provides a means of understanding these general influences of the vortex dynamics.

Figure 12 shows the results of the integral model with the turbulent intensity (3.13) being defined at a distance $x > X_f$ (for $X_f = 5R_0$), consistent with the numerical model of a spherical vortex moving through a quiescent region prior to penetrating the decaying turbulence. The predicted trend for the velocity and position (figure 12a,c), as a function of time, show quite similar trends to the numerical model, in particular the abrupt change in the vortex speed as it penetrates into the turbulent region. The reduction of the vortex speed is a consequence of the loss of vortical fluid (reducing impulse) and entrainment that causes the vortex size to grow. As is evident from figures 7(a) and 10, the increase in the vortex radius is less than 50% during the rapid decrease in vortex speed. The later stage of the spherical vortex dynamics, where $U_v/u_e < \lambda_c$, is characterised by the vortex essentially stopping and spreading rapidly in a diffusive manner, a process that is not captured by the integral model. The critical ratio λ_c can be approximately determined from figure 9(b) to be $\lambda_c \sim 3$, while the experimental results (figure 11) suggest $\lambda_c \sim 5$.

Figure 13 shows the penetration distance of a vortex vs the inverse strength of the turbulence, for the experiments, numerical simulations and the integral model. The legend lists the specific configuration for the integral model, with the start of the turbulent

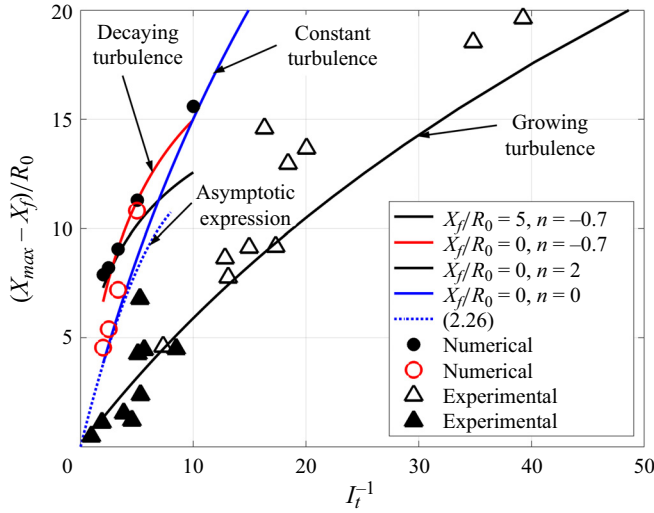


Figure 13. The variation of the penetration distance into turbulence ($X_{max} - X_f$) is plotted against the inverse of turbulent intensity, I_t , with the results determined by experiments, computations and the integral model. For the experimental study, I_t is defined by (4.4). The results from the integral model are plotted as full curves and the decay law and turbulent front as listed in the legend. The numerical results are for the case of a vortex starting in turbulence (\circ , red) or moving into turbulence (\bullet). The experimental results are distinguished between weak and strong vortices, \blacktriangle and \triangle , respectively. The asymptotic expression (2.26) for strong turbulence is compared against the integral model for sustained turbulence.

region and exponent for the turbulence growth listed. Three configurations are listed, specifically decaying turbulence ($n = -0.7$), sustained turbulence ($n = 0$) and growing turbulence ($n = 2$), with the later chosen to mimic the scenario of the vortex moving into progressively stronger turbulence that occurs in the experiments.

The curves for decaying turbulence show the vortex penetration distance at $t = 50R_0/U_{v0}$, while the remaining curves describe the ultimate penetration distance. The numerical simulations were repeated with the vortex starting in turbulence ($X_f/R_0 < 0$) to contrast the case of a vortex moving into turbulence ($X_f/R_0 = 5$). Starting in turbulence meant that its influence on the vortex dynamics was rapid, reducing the penetration distance, giving a consistent trend similar to the integral model, with the distance varying approximately with I_t^{-1} . The initial turbulence also affected the vortex stability

For turbulence whose intensity is sustained, the integral model recovers the asymptotic result (2.26), where the penetration distance scales with I_t^{-1} . This approximately linear trend is also evident in the experimental results. There is scatter in measurements of the penetration distance for intense turbulence (high I_t) which is expected when the spherical vortex starts to interact with coherent structures shed from the oscillating bars. The integral model is shown for $n = 2$, where the vortex moves into a region of turbulence whose strength progressively increases in time. Although this does not match the spatial dependence seen in figure 3, it does highlight the significant reduction of the penetration distance (compared with decaying and forced turbulence) with a trend quite similar to the experimental observations.

7. Conclusion

This paper provides a detailed theoretical and experimental study of the arrestment of a spherical vortex penetrating a region of turbulence. The complexity of the new elements required a combination of different techniques to unravel the key physics.

An integral perspective of vortex dynamics in quiescent flow is able to reconcile the far-field dipolar nature of the vortex flow with the near-field source flow generated by entrainment and impulse loss. This result also holds for vortices moving in turbulence because the turbulence is generally characterised by a negligible total impulse. The vortex model of Maxworthy (1977) is extended to account for the effect of external turbulence in terms of increased entrainment and reconciles the results from the numerical and experimental studies. A modest level of background turbulence causes the vortex to slow down more rapidly and grow faster, leading to a finite penetration distance that scales with I_t^{-1} . Ultimately, the vortex speed becomes comparable to the external turbulence, after which the vortex stops and rapidly spreads as it is dispersed by the ambient turbulence. The evolution the vortex has been assessed by tracking a large number of fluid particles. This Lagrangian technique turns out to be a fruitful technique for understanding vortex–turbulence interactions in the future. The consistent feature of the experimental and theoretical model is the small growth rate of the vortex but a significant increase in the loss of vortical fluid at the rear.

The paper has examined the impact of external turbulence on the vortex from an integral perspective, specifically analysing the vortex’s movement and determining the penetration distance. The distortion and modification of external turbulence are complex phenomena. Disentangling these general flow processes will be the focus of our future research efforts.

Acknowledgements. The authors would like to thank C. Bordier for managing the exchange between University College London and LEGI, and K. van der Lee for supporting a preliminary experimental investigation during his internship at LEGI. The authors acknowledge the use of the UCL Kathleen High Performance Computing Facility (Kathleen@UCL), and associated support services, in the completion of this work.

Funding. This work is supported by the French National Research Agency in the framework of Tec21 of the France 2030 program ANR-15-IDEX-0002.

Declaration of interests. The authors report no conflict of interest.

Author ORCIDs.

 Ian Eames <https://orcid.org/0000-0002-1300-5738>;

 Jan-Bert Flór <https://orcid.org/0000-0002-7114-2263>.

REFERENCES

- ABRAMOWITZ, M. & STEGUN, I.A. 1964 *Handbook of Mathematical Functions with Formulas, Graphs, and Mathematical Tables*, 9th dover printing, 10th gpo printing edn. Dover.
- ARNOLD, O. 1974 Wirbelringe in turbulenzarmer und turbulenter Umgebung. PhD thesis, University of Karlsruhe.
- ARNOLD, O., KLETTNER, C.A. & EAMES, I. 2013 Vortex rings moving into turbulence. *J. Turbul.* **14** (1), 190–202.
- BENJAMIN, T.B. & ELLIS, A.T. 1966 The collapse of cavitation bubbles and the pressures thereby produced against solid boundaries. *Phil. Trans. R. Soc. Lond. A* **260** (1110), 221–240.
- CAMASSA, R., KHATRI, S., MCLAUGHLIN, R., MERTENS, K., NENON, D., SMITH, C. & VIOTTI, C. 2013 Numerical simulations and experimental measurements of dense-core vortex rings in a sharply stratified environment. *Comput. Sci. Discov.* **6** (1), 014001.
- COELHO, S.L.V. & HUNT, J.C.R. 1989 The dynamics of the near field of strong jets in crossflows. *J. Fluid Mech.* **200**, 95–120.
- DARWIN, C. 1953 Note on hydrodynamics. *Math. Proc. Camb. Phil. Soc.* **49** (2), 342–354.
- EAMES, I. 2008 Disappearing bodies and ghost vortices. *Phil. Trans. R. Soc. Lond.* **366** (1873), 2219–2232.
- EAMES, I., BELCHER, S.E. & HUNT, J.C.R. 1994 Drift, partial drift and Darwin’s proposition. *J. Fluid Mech.* **275**, 201–223.
- EAMES, I. & FLOR, J.B. 1998 Fluid transport by dipolar vortices. *Dyn. Atmos. Oceans* **28** (2), 93–105.

- EAMES, I. & HUNT, J.C.R. 2004 Forces on bodies moving unsteadily in rapidly compressed. *J. Fluid Mech.* **505**, 349–364.
- EAMES, I., HUNT, J.C.R. & BELCHER, S.E. 2004 Inviscid mean flow through and around groups of bodies. *J. Fluid Mech.* **515**, 371–389.
- FUNG, J.C.H., HUNT, J.C.R., MALIK, N.A. & PERKINS, R.J. 1992 Kinematic simulation of homogeneous turbulence by unsteady random Fourier modes. *J. Fluid Mech.* **236**, 281–318.
- GHARIB, M., RAMBOD, E. & SHARIFF, K. 1998 A universal time scale for vortex ring formation. *J. Fluid Mech.* **360** (0), 121–140.
- HILL, M.J.M. 1894 On a spherical vortex. *Phil. Trans. R. Soc. Lond. A* **185**, 213–245.
- HOPFINGER, E.J. & TOLY, J.-A. 1976 Spatially decaying turbulence and its relation to mixing across density interfaces. *J. Fluid Mech.* **78** (1), 155–175.
- HUNT, J.C.R. & EAMES, I. 2002 The disappearance of laminar and turbulent wakes in complex flows. *J. Fluid Mech.* **457**, 111–132.
- HUNT, J.C.R., WRAY, A.A. & MOIN, P. 1988 Eddies, streams, and convergence zones in turbulent flows. In *Proceeding of the Summer Program 1988 in Center for Turbulence Research*, pp. 193–208.
- VAN JAARVELD, J.P.J., HOLTEN, A.P.C., ELSENAAR, A., TRIELING, R.R. & VAN HEIJST, G.J.F. 2011 An experimental study of the effect of external turbulence on the decay of a single vortex and vortex pair. *J. Fluid Mech.* **670**, 214–239.
- KRAICHNAN, R.H. 1959 The structure of isotropic turbulence at very high Reynolds numbers. *J. Fluid Mech.* **5** (4), 497–543.
- LOVALENTI, P.M. & BRADY, J.F. 1993 The hydrodynamic force on a rigid particle undergoing arbitrary time-dependent motion at small Reynolds number. *J. Fluid Mech.* **256**, 561–605.
- MARSHALL, J.S. & BENINATI, M.L. 2005 External turbulence interaction with a columnar vortex. *J. Fluid Mech.* **540** (1), 221–245.
- MAXWORTHY, T. 1974 Turbulent vortex rings. *J. Fluid Mech.* **64**, 227–239.
- MAXWORTHY, T. 1977 Some experimental studies of vortex rings. *J. Fluid Mech.* **81**, 465–495.
- MOORE, D.W. 1963 The boundary layer on a spherical gas bubble. *J. Fluid Mech.* **16** (2), 161–176.
- MORTON, B.R., TAYLOR, G. & TURNER, J.S. 1956 Turbulent gravitational convection from maintained and instantaneous sources. *Phil. Trans. R. Soc. Lond. A* **234** (1196), 1–23.
- POULAIN-ZARCOS, M., MERCIER, M.J. & HALLE, A. 2022 Global characterization of oscillating grid turbulence in homogeneous and two-layer fluids, and its implication for mixing at high Péclet number. *Phys. Rev. Fluids* **7** (5), 054606.
- PULLIN, D.I. & SAFFMAN, P.G. 1998 Vortex dynamics in turbulence. *Annu. Rev. Fluid Mech.* **30**, 31–51.
- VAN REEUWIJK, M. & CRASKE, J. 2015 Energy-consistent entrainment relations for jets and plumes. *J. Fluid Mech.* **782**, 333–355.
- SAFFMAN, P.G. 1995 *Vortex Dynamics*. Cambridge University Press.
- SAFFMAN, P.G. 1997 Vortex models of isotropic turbulence. *Phil. Trans. R. Soc. Lond. A* **355** (1), 1949–1956.
- DA SILVA, C.B., HUNT, J.C.R., EAMES, I. & WESTERWEEEL, J. 2014 Interfacial layers between regions of different turbulence intensity. *Annu. Rev. Fluid Mech.* **46** (1), 567–590.
- SYNGE, J.L. & LIN, C.C. 1943 On a statistical model of isotropic turbulence. *Trans. R. Soc. Can.* **37**, 145–79.
- THEODORSEN, T. 1941 Impulse and momentum in an infinite fluid. In *Von Kármán Anniversary Volume*, pp. 49–57. California Institute of Technology.
- TINAIKAR, A., ADVAITH, S. & BASU, S. 2018 Understanding evolution of vortex rings in viscous fluids. *J. Fluid Mech.* **836**, 873–909.
- VERZICCO, R., FLOR, J.B., VAN HEIJST, G.J.F. & ORLANDI, P. 1995 Numerical and experimental study of the interaction between a vortex dipole and a circular cylinder. *Exp. Fluids* **18**, 153–163.
- WIDNALL, S.E. & SULLIVAN, J.P. 1973 On the stability of vortex rings. *Proc. R. Soc. Lond. A* **332** (1590), 335–353.
- WILCZEK, M., DAITCHE, A. & FRIEDRICH, R. 2011 On the velocity distribution in homogeneous isotropic turbulence: correlations and deviations from Gaussianity. *J. Fluid Mech.* **676**, 191–217.